Small angle X-ray scattering overlay metrology for advanced nodes

Timothée Choisnet, Yoann Blancquaert, Guillaume Freychet, Patrice Gergaud

Small angle X-ray scattering overlay metrology for advanced nodes

Timothée Choisnet[a, *], Guillaume Freychet[a], Yoann Blancquaert[a] and Patrice Gergaud[a]

[a] *Univ. Grenoble Alpes, CEA, Leti, F-38000 Grenoble, France*;

ABSTRACT

With a sub-nanometric resolution required for nodes below 14 nm, according to the International Roadmap for Devices and Systems (IRDS), exploring new overlay characterization methods is key to drive further component size reduction and develop better-performing technologies. In this work, we present our first Small-Angle X-ray Scattering (SAXS) results of overlay measurements on stacks of silicon line gratings. Our method, novel for SAXS overlay measurements, is based on inverse problem resolution and reconstructs the in-depth profile (approximated as a stack of trapezoids) of the structure. We are thus able to extract overlay with SAXS with a very fine sensitivity, high precision and sub-nanometric resolution that suit the requirements for advanced technological nodes. We compared these results with those of Scanning Electron Microscopy (SEM) contour-based on product overlay. The reconstructed structures are compared to profiles obtained with Scanning Transmission Electron Microscopy (STEM). From the differences between these multi-scale techniques we can conclude on the high potential of SAXS to become a complementary to those existing, and assess its potential for advanced technology nodes.

Keywords: overlay, Small-Angle X-ray Scattering, contour-based overlay, scanning transmission electron microscopy.

* Corresponding author. Contact: timothee.choisnet@cea.fr

1. INTRODUCTION

In order to meet with constantly more demanding specifications in term of feature size and performances, the integrated circuits have been evolving with the use of complex 3D structures, new materials, patterning techniques and processes [1]. With such evolutions come metrological challenges for the measurement of defectivity, Critical Dimension (CD), material properties and overlay, which particularly remains a constraint in increasing device yield with its continually shrinking budget [2,3].

Optical techniques such as Image Based Overlay (IBO) and Diffraction Based Overlay (DBO) are commonly used for overlay metrology. The main challenges lie in the design of small and process-representative targets which has driven the research for the past decade [4–7]. The usage of dedicated targets causes a lack of measurements statistics and, despite the efforts of the industry, representativeness of the process. This has led to the investigation of on-product overlay measurements, with techniques such as scatterometry and contour-based Scanning Electron Microscopy (SEM) overlay [8–11], as complementary measurements to optical overlay.

On the other hand, the increasing need of high resolution for CD metrology has led to the emergence of CD-Small Angle X-ray Scattering (CD-SAXS), a technique proven efficient for the reconstruction of patterns with sub-nanometric resolution [12–14]. Reche *et al.* also developed the method for line edge roughness measurement [15,16]. SAXS however lacks of powerful sources to be fit to structures others than High Aspect Ratio (HAR) in High Volume Manufacturing (HMV) [17–19], and sources 100 times brighter than conventional rotating anode sources are needed according to the International Roadmap for Devices and Systems (IRDS) [1].

In this study we develop a method for overlay measurement with SAXS. In 2018, Veldman *et al.* enlightened a method of extraction based on the displacement of intensity minima in the scattering diagram of a sample [20]. More recently, Zhang *et al.* proposed a similar method but with a limited number of sample rotations, using reciprocal space slicing (RSS) [21]. Here we propose our methodology for the extraction that allows the extraction of other parameters in complement to the overlay. We designed samples compatible with SEM, Scanning Transmission Electron Microscopy (STEM) and SAXS. We compare the overlays measured and the structures reconstructed between these techniques, and state on our method's validity.

2. METHODS

2.1 Samples

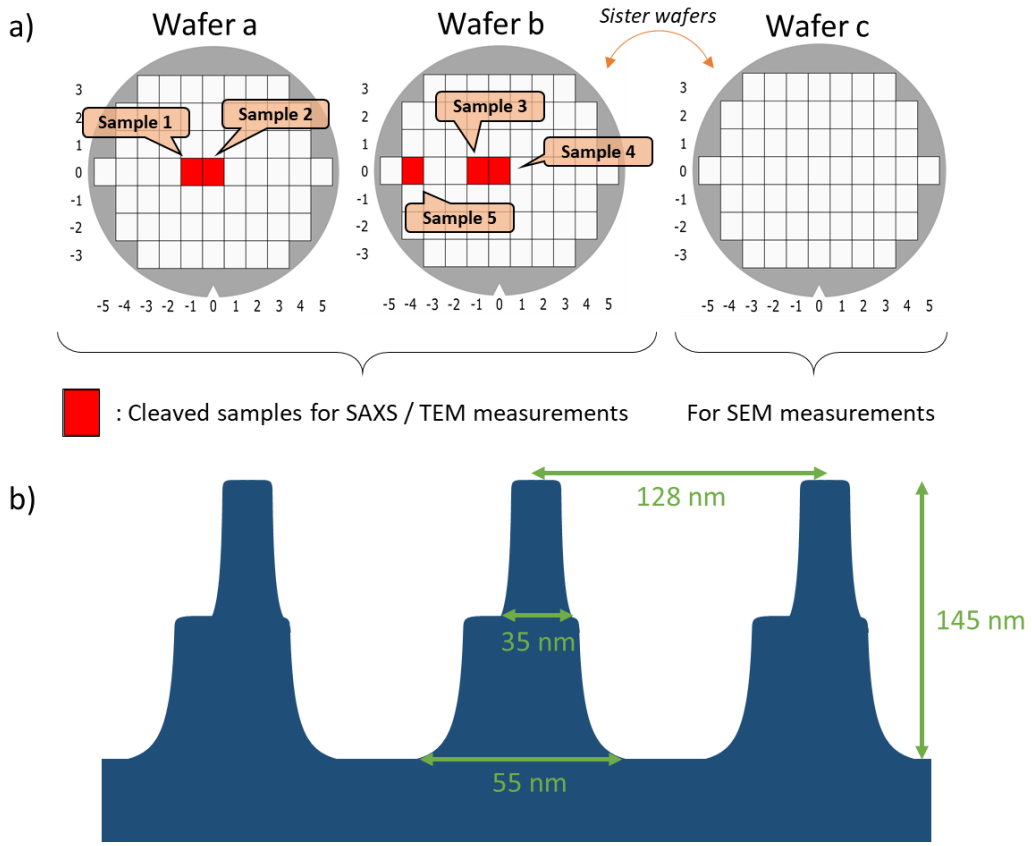

Figure 1. a) Description of the process flow and b) scheme of the strong-castle structures studied.

Our samples, fabricated at CEA Leti, consist of large arrays (1 mm × 1.5 mm) of silicon lines gratings stacks. The mask used contains two "complementary" zones spaced by 85 µm in the y-direction: one presents 80 nm CD lines spaced by 48 nm, and the complementary 48 nm CD lines spaced by 80 nm. A first patterning step with 193i lithography and dry etching was performed to obtain the bottom trapezoids. The mask was then shifted to align the complementary structures and the same patterning steps were performed to obtain our so-called "strong-castle" structures displayed in Figure 1b. As shown on Figure 1a, three wafers were processed (labelled a, b and c). The process conditions were similar and the wafers were fabricated successively. Programmed overlays were introduced in the x-direction by setting controlled shifts to the scanner along the lithographic field. For the wafer a, the expected overlay ranges aimed were from 10 nm (left of the wafer) to -10 nm (right of the wafer) with a step of 2 nm to obtain a 0 nm overlay in the center column. The wafers b and c were processed to obtain a range from 5 to -5 nm (left to right on the wafer) with a step of 1 nm to obtain, again, 0 nm overlay on the center column.

A total of 5 samples with various overlay values were obtained, labeled from "sample 1" to "sample 5". The strong castles are spaced by a 128 nm constant pitch. The critical dimension (CD) of the bottom trapezoid is 55 nm, while the one of the top trapezoid is set to 35 nm. Each trapezoid is 70 nm high, yielding a total height of 140 nm to the structure.

2.2 Workflow and measurement techniques

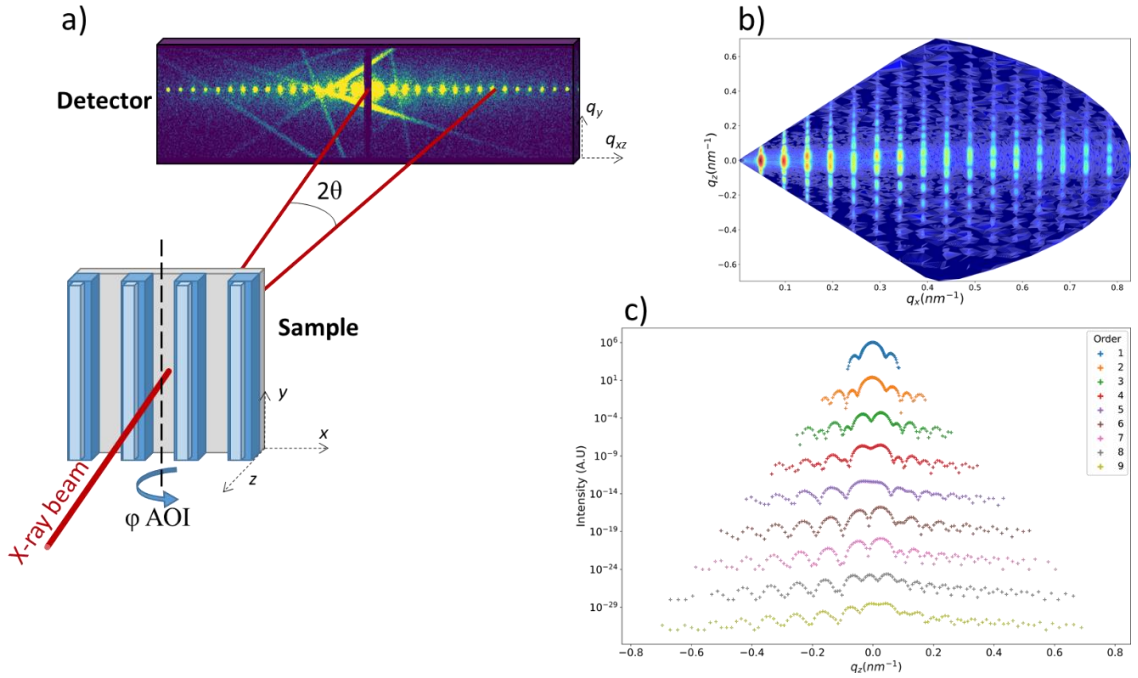

Figure 2. a) illustration of SAXS measurements performed in transmission geometry, b) resulting reciprocal space map (RSM) and c) intensity profiles extracted along q_z for each Bragg peak position along q_x.

STEM specimens were prepared by focused ion beam milling. The STEM measurements were then performed using a probe corrected FEI Titan Ultimate operated at 200 kV. High angle annular dark field (HAADF) STEM images were acquired in the regions of interest. Length calibration is performed on each sample by measuring the interatomic distances across several unit cells on the silicon substrate. Samples 2 to 5 were imaged, with an image at the center of the 1.5 mm × 1 mm zone to match with the zones probed with the other techniques.

SEM images were taken on a Verity 6i (AMAT) tool. The acceleration voltage used is 1600 V for a 10 pA probe current, with a pixel size of 0.6 nm × 0.6 nm. A field of view (FoV) of 0.71 µm × 0.64 µm was recorded to ensure there were at least 5 lines on each image. For each sample, the final images used for data treatment are obtained by averaging the 3 lines recorded simultaneously at each acquisition. The scan rate was set to 3xTV for 20 frames per image. The images were then treated on SIMPL software, developed by Aselta (AMAT) and adapted for our needs at CEA Leti. The overlay extraction on SIMPL is detailed further in the document. We performed 30 measurements per lithographic field the wafer c (Figure 1a)

CDSAXS experiments were performed at the Soft Matter Interfaces Beamline (SMI, Beamline 12-ID) at the National Synchrotron Light Source (NSLS) II with a photon energy of 16100.0 ± 1.6 eV to enable a 24.2 % transmission of the X-rays through the 775-µm thick silicon wafer at normal incidence, dropping to 5.5 % at the maximum sample rotation φ = ± 60°. Scattered intensity is recorded with Pilatus3 1M which is positioned at 8300 ± 2 mm from the sample, calibrated by measurements on a reference sample. SAXS patterns were recorded at different rotation angles φ from -60 degrees to +60 degrees with a step of 1 degree along the *y*-axis (Figure 2a), with an exposure time of 1 second per φ angle . The 2D images were corrected by a 2D background image acquired on a blank silicon zone for the same φ range. This rotation around φ allows the decomposition of the scattering vector $q_{x,z}$ into two distinct vectors $q_x = q_{x,z}\cos(\varphi)$ and $q_z = q_{x,z}\sin(\varphi)$. Each image was integrated vertically along $q_y = 0$ Å^{-1} and a reciprocal space map (RSM) on (q_x, q_z) was obtained and shown on Figure 2b. Each 1D profile obtained from the vertical integration at each φ was used to extract the mean and amplitude of the nine first Bragg orders. Using a Gaussian model, the $q_{x,z}$ and intensity of each peak were extracted. These extracted intensities are then corrected given the sample rotation, the substrate thickness and its attenuation factor. They are then plotted on the sample's scattering diagram (Figure 2c) and will be used as the experimental dataset in the fitting procedure described later on.

The transmission geometry allows relatively small beam footprint of 250 µm × 25 µm at normal incidence up to 500 µm × 25 µm at maximum sample tilt. The samples were measured 5 times with SAXS to obtain a static repeatability and evaluate so the technique's precision.

Our method for overlay metrology using SAXS, based on inverse problem solving, does not differ much from the method used for CD, height or SWA measurements.

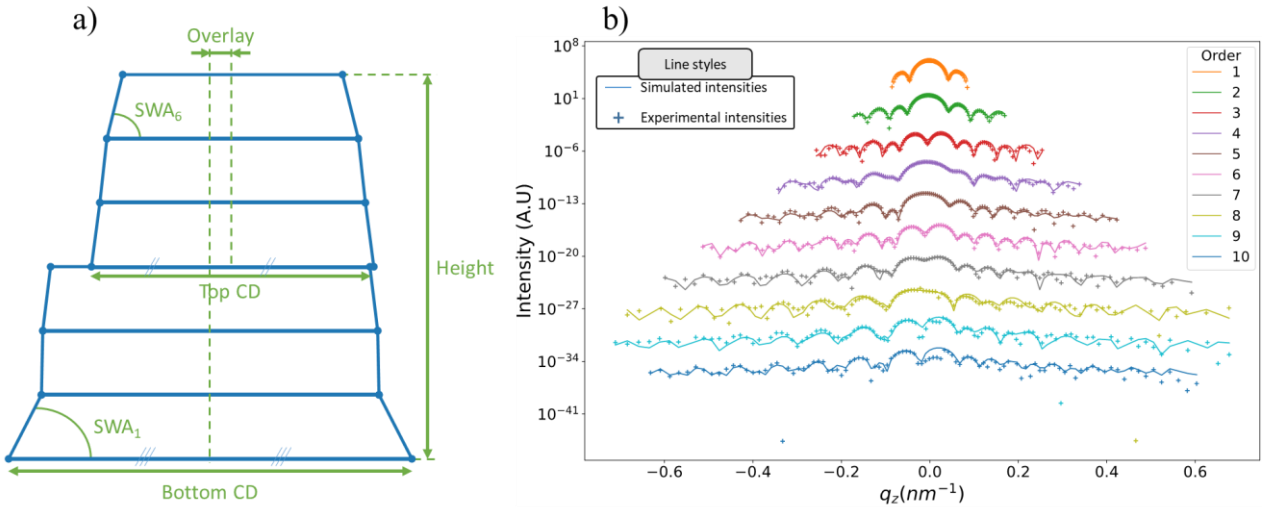

Figure 3.a) Description of the "strong-castle" model used for SAXS iterative resolution and b) comparison between experimental ("+" scatter plot) and simulated (line plot) reciprocal space cartographies.

Here we decide to describe the line profile as a stack of trapezoids (Figure 3a), which are themselves discretized into N sub-trapezoids. This discretization of line gratings into trapezoids has been proven efficient for the reconstruction of line gratings structures [12,30,31], and the STEM images which will be discussed later on confirm that it is appropriate. We chose here to discretize with a total of $N = 6$ sub-trapezoids with a constant height. The floating geometrical parameters are the bottom CD, top CD (which is actually the bottom CD of the top trapezoid), two SWAs for each sub-trapezoid (which are chosen to be symmetrical), the height and the overlay, resulting in 10 floating parameters. The Fourier transform is calculated for each sub-trapezoid n with the equation 1 adapted from [32].

$$F_n(q_x, q_z) = \frac{1}{q_x}\left[-\frac{m_{1,n}}{t_{1,n}}\, e^{-i\,q_x\left(offset-\frac{L_n}{2}\right)}\left(1-e^{-i\,h\left(\frac{q_x}{m_{1,n}}+q_z\right)}\right)+\frac{m_{2,n}}{t_{2,n}}\, e^{-i\,q_x\left(offset+\frac{L_n}{2}\right)}\left(1-e^{-i\,h\left(\frac{q_x}{m_{2,n}}+q_z\right)}\right)\right] \quad (1)$$

In this equation, $m_1 = \tan(SWA_{n,left})$, $m_2 = \tan(\pi - SWA_{n,right})$, L_n is the bottom linewidth of the n^{th} trapezoid, h is the height of each trapezoid (kept constant to simplify) and $t_{i,n} = q_x + m_{i,n}q_z$. The $offset$ takes only two values: 0 nm for the 3 sub-trapezoids that describe the bottom trapezoid (which is the reference and thus centered on 0) and the overlay for the 3 sub-trapezoids describing the top one. The Fourier transform of the whole tessellation is then given by equation 2 below:

$$F(q_x, q_z) = \sum_{n=1}^{N} F_n(q_x, q_z) e^{i\,n\,h\,q_z} \quad (2)$$

The scattered intensity $I = |F(q_x, q_z)|^2$ is used to reconstruct the model's scattering diagram. A comparison between the simulated and experimental data is plotted on Figure 3b. We iterate over these floating parameter and try to minimize the logarithmic error between the simulated and the measured scattering diagrams (Figure 3b), which is our metric for goodness of fit (GOF) estimation. We use a covariance matrix adaptation evolution strategy (CMAES) proposed by Hannon *et al.* [33] with the DEAP python library [34]. Hansen et Ostermeier [35] proposed lower bounds for the population

size λ and mutational rate μ to use, given the number N of floating parameters. The population size was thus set to 100 (significantly greater than the $\lambda = int(4 + 3ln(N)) = 12$ recommendation) and μ was set to 30, satisfying the $\mu \leq {}^{\lambda}/_{2}$ recommendation. A great population size is necessary in order to improve the search of a global minimum and avoid local minima as best as possible. When the number of iteration reaches 1000 or when the GOF is low enough, the process is ended. To evaluate the ability of the algorithm to avoid local minima, the fitting procedure was operated 50 consecutive times on one dataset, randomizing the initial parameters in the ± 10% range around the values taken for standard fitting.

2.3 SEM overlay extraction on SIMPL

SEM based overlay or edge placement metrology has been the subject of many researches and publications [10,22–27]. SIMPL is a model-based contour extraction software that has been proven to be robust to noise, both random and systematic (such as noise and charging) [28]. The first step is the generation of a seed from a known layout of the structure, and its alignment on the image with algorithms such as cross-correlation [29]. Gauges are then placed on the seed, with tunable parameters such as the detection rate, the gauge length and orthogonal/longitudinal filters that aim to smoothen irregularities and improve noise robustness. The contour of the structure is then extracted based on the grey levels of the image. As for SEM images, contours can be extracted at different levels of the signal (Figure 4a, b): maximum, minimum, max slope (i.e 80% of the maximum) and max slope reversed (80% of the maximum on the negative slope). Several measurements can then be performed with the extracted contour: the CD, centroid, pitch, perimeter … The extraction was tested and validated on a sample and then generalized to our whole batch of measurements.

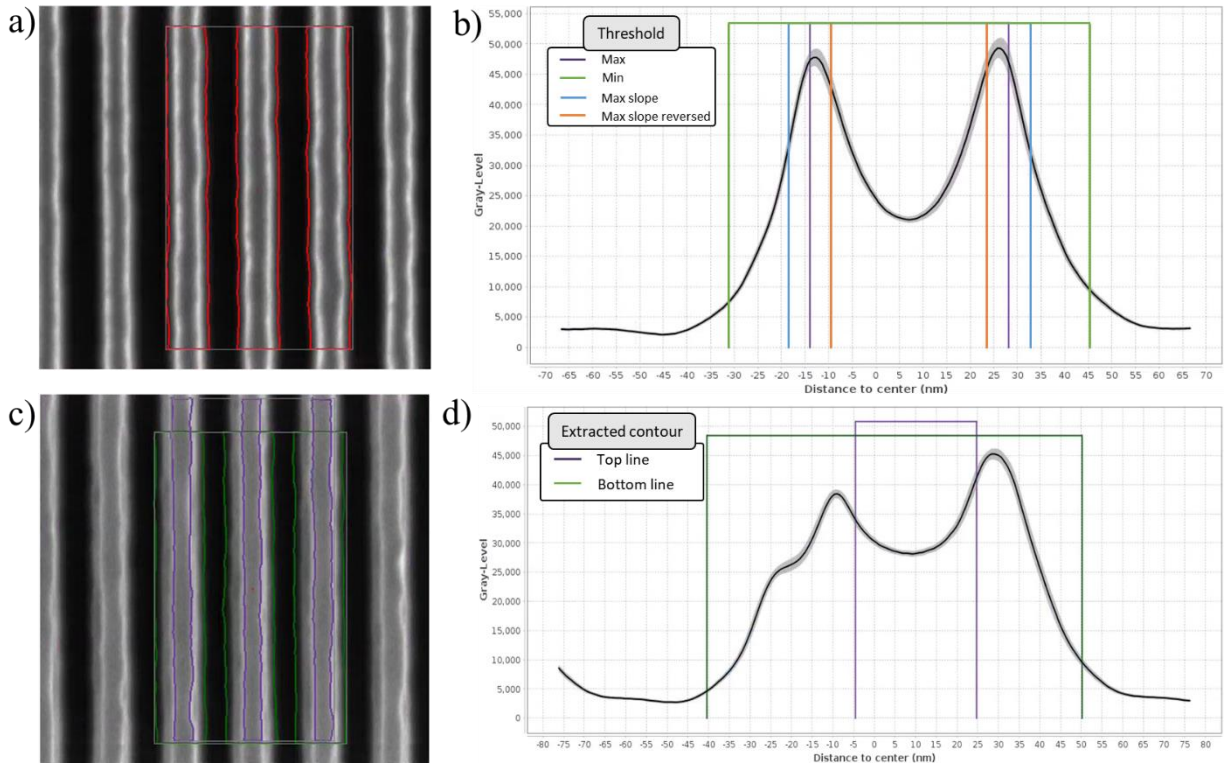

Figure 4. Top figures show the impact of the threshold on the extraction: a) displays the extracted contours of a SEM image with the "min" threshold and b) shows the where each algorithm extracts the contour on the grey-level signal. Bottom figures show how to utilize the threshold to extract the contours of two contours on top of each other : c) a SEM image of one of our structures and d) extraction of their contours with "max slope reversed" algorithm for top line and "min" algorithm for the bottom line.

This method allows on-product measurements [10] and is of great interest to reduces the non-zero overlay (NZO), defined by the offset between on-product overlay (OPO) and the overlay commonly measured on dedicated targets with Image Based-Overlay (IBO) and Diffraction Based Overlay (DBO).

Our samples consist on a stack of 2 line gratings. As shown on Figure 4c and d, the contour extraction is thus separated in two parts: one for the top line, another one for the bottom line. The centroid difference is then computed to obtain the overlay. An in-house developed plugin allows the repetition of this extraction on our whole batch of measurements. The lines being directly on top of each other, it sometimes is hard to differentiate them. Our top and bottom lines CDs being relatively close to each other and our overlay values being low, the grey level signal can sometimes not display clearly the separation of the two lines, as it is the case in Figure 4a, b for example. This can lead to errors of contour extractions that cannot be solved even with a right tuning of gauge length and smoothing. To make sure we extract the contour of the right line each time, we use different detection thresholds: "min" for the bottom line and "max slope reversed" for the top one (Figure 4b). This implies an assumption that the lines are symmetrical regarding their center.

3. RESULTS

3.1 SEM and SAXS comparison

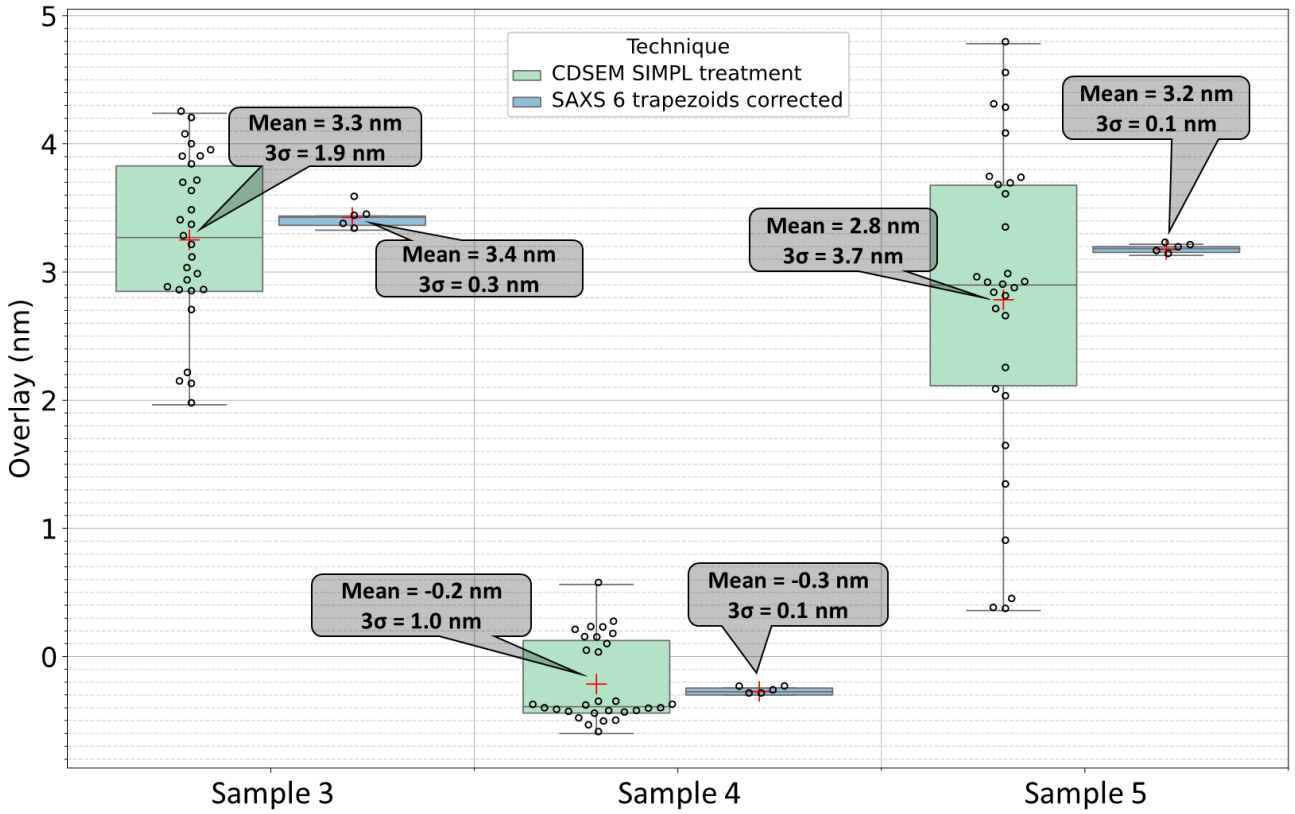

Figure 5. Overlays measured on samples 3 to 5 (and equivalent on sister wafer) with SAXS and SEM.

Figure 5 shows the results obtained with SEM and SAXS on the samples 3, 4 and 5 and (for SAXS) and the corresponding ones on the sister wafer for SEM. The data are represented with a superposition of boxplots and scatterplots. This allows the visualization of statistics (mean, median value, inter quartile range) and the distribution of the values. We use the 3σ distribution around the average value to express the measurement uncertainty. One can see that the techniques agree well, with differences ranging from 0.1 nm to 0.4 nm. The 3σ distribution of SAXS measurements ranges from 0.1 nm to 0.3 nm, which shows that the technique's experimental setup is stable and leads to repeatable parameters extraction. However, more measurements should be made to enhance the statistics and have a more accurate calculation of the 3σ distribution. SEM measurements have distributions that are much more spread, ranging from 1.0 nm to 3.7 nm. One can also see that the measurements are located in several clusters for sample 4 and 5. This could be explained partly by a lack of stability in the extraction, but also a great part could be the local character of the measurements. We indeed measure three lines per SEM image while we average over 25 µm × 500 µm with SAXS. We chose to take 30 SEM images over the SAXS spot to measure the same zones with both techniques, but SEM is sensitive to local overlay variations while SAXS extracts an

average value. This could explain why the average values are close between the techniques, while SEM has a wide dispersion.

3.2 STEM images and SAXS reconstruction comparisons

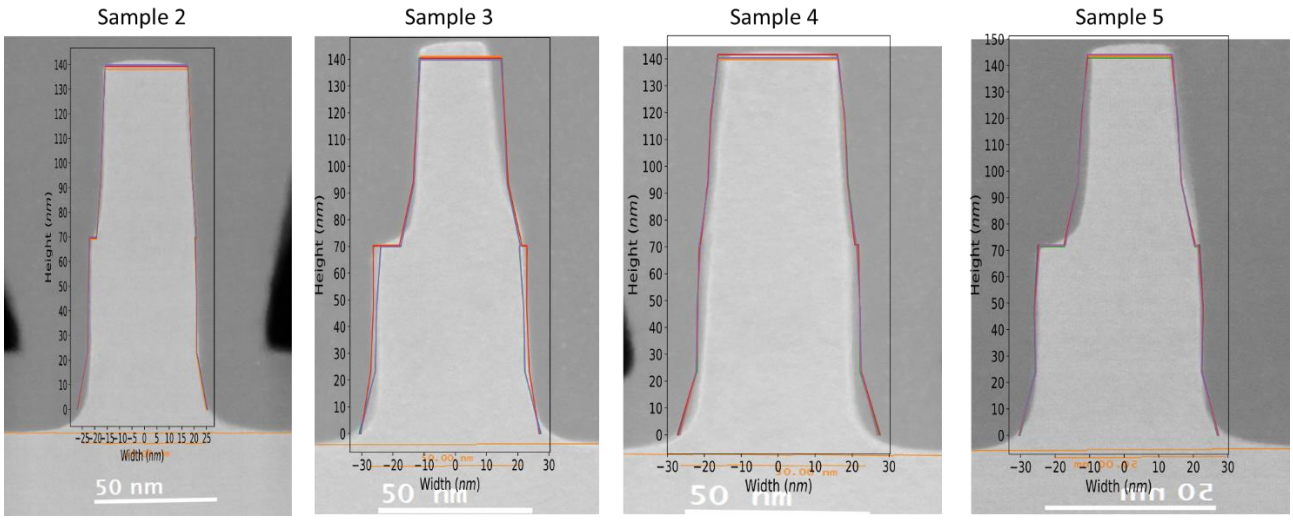

Figure 6. Superposition of STEM images and SAXS shape reconstruction of samples 2 to 5.

Figure 6 shows the superposition of STEM images and the 5 repeatability reconstructions measured with SAXS on corresponding samples. One can see that the profiles overlap very well. Even though STEM images are extremely local compared to SAXS (1 line compared to an average over 500 µm × 25 µm surface), this good agreement is encouraging and shows that SAXS can rebuild a structure with overlay, and more importantly provides a sub nanometric overlay with good enough accuracy as shown on Figure 6. Improvements of SAXS model could lead to a better matching with STEM images: for example, on sample 5 we see that our symmetrical model limits the left part of the top trapezoid. We could also implement a model with rounded corners at the top and bottom of the trapezoids, which has shown efficient for CD measurement on prior works [31].

4. DISCUSSION

4.1 SAXS and SEM overlay measurements comparison

We observe a large 3σ distribution of the SEM overlays measured. This can be due to the fact that our contour extraction is not perfectly calibrated yet. The strong castle structures observe allow us to see the 2 levels of line gratings, but their respective contours cannot be perfectly distinguished as can be seen on Figure 4. This leads to many restrictions in the parameters chosen for alignment, contour extraction and measurement. The 2 clusters of solutions observed on repeatability measurements (Figure 5) show the instability of our method. Strong castles with a greater difference in CDs between the top and bottom trapezoids must be processed to have better results. SAXS shows promising results.

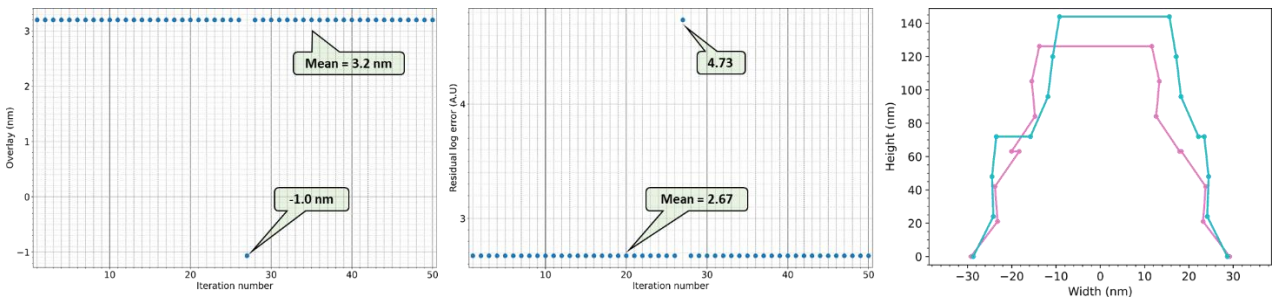

Figure 7. 50 SAXS extraction on the same dataset (sample 8, repetition n°1) and resulting a) overlays and b) residual log error. The overlapped 50 lineprofiles are plotted on sub figure c).

Figure 7 shows 50 repeated extractions on the same dataset (sample 5, first repetition measurement), with a random initiation of the initial parameters at each iteration in the ± 10 % range around their nominal values. The overlays and the residual log errors (our metric for the GOF) are displayed. One can see that the extraction is highly stable: over 50 extractions, only one (extraction number 26) falls into a local minimum resulting in a GOF of 4.73 instead of the 2.67 obtained with the other extractions. The impact on the overlay can also be seen: we extract a – 1.0 nm overlay when this error occurs against the 3.2 nm obtained when reaching the global minimum. As shown by Figure 7c, all the other geometrical parameters are extremely stable, and the reconstructed strong castle when the fit is stuck in a local minimum has nothing to do with those reconstructed with the global minimum. Despite the one reconstruction over 50 that did not fit correctly, the model and the fitting procedure show to be efficient and stable.

5. CONCLUSIONS

SAXS is a well known and robust technique for CD measurements. In this study, thanks to a novel method of overlay extraction, we demonstrate that SAXS is also pertinent and robust for overlay metrology for advanced technology nodes. A sub-nanometric resolution with an excellent stability in extraction are obtained through the reconstruction of a whole pattern by inverse problem solving. Our SAXS reconstruction of structures with overlay show a significant matching with SEM contour-based overlay metrology and an excellent overlapping with STEM images. Further investigations are needed to obtain more statistics on SAXS measurements. Also, the comparison with conventional IBO and DBO techniques is also required before considering SAXS as an overlay reference technique. Extension to more complex structures (coating and stacks with various materials) is also necessary to determine the technique's potential.

ACKNOWLEDGEMENTS

This research used the Soft Matter Interfaces Beamline (SMI, Beamline 12-ID) of the National Synchrotron Light Source II, a U.S. Department of Energy (DOE) Office of Science User Facility operated for the DOE Office of Science by Brookhaven National Laboratory under Contract No. DE-SC001270.

The data that support the findings of this article are not publicly available due to privacy. They can be requested from the corresponding author.

STEM characterizations were carried out on the Platform for Nanocharacterisation (PFNC), supported by the "Recherche Technologique de Base" and "France 2030 - ANR-22-PEEL-0014" programs of the French National Research Agency (ANR)

We warmly thank Jorge Nacenta Mendevil and Aurélien Sarrazin for their help and our discussions during the processing of these samples.

REFERENCES

[1] International Roadmap for Devices and Systems, Metrology, 2023 edition, IEEE International Roadmap for Devices and Systems TM, 2023.

[2] B.D. Bunday, A. Bello, E. Solecky, A. Vaid, 7/5nm logic manufacturing capabilities and requirements of metrology, in: O. Adan, V.A. Ukraintsev (Eds.), Metrol. Insp. Process Control Microlithogr. XXXII, SPIE, San Jose, United States, 2018: p. 17. https://doi.org/10.1117/12.2296679.

[3] N.G. Orji, M. Badaroglu, B.M. Barnes, C. Beitia, B.D. Bunday, U. Celano, R.J. Kline, M. Neisser, Y. Obeng, A.E. Vladar, Metrology for the next generation of semiconductor devices, Nat. Electron. 1 (2018) 532–547. https://doi.org/10.1038/s41928-018-0150-9.

[4] S. Katz, N.A.K. Roy, S. McCandless, J. Reece, N. Gillespie, N. Monserud, Y. Grauer, M. Stakely, G. Gray, Y. Li, P. Kimani, N. Park, I. Yasuhisa, I. Koichi, I. Kosuke, Y. Zhang, OPO robustness and measurability improvement via extended wavelengths, in: Metrol. Insp. Process Control XXXVII, SPIE, 2023: pp. 300–307. https://doi.org/10.1117/12.2655161.

[5] Y. Blancquaert, C. Dezauzier, J. Dépré, M. Miqyass, J. Beltman, Performance of ASML YieldStar μDBO overlay targets for advanced lithography nodes C028 and C014 overlay process control, in: San Jose, California, USA, 2013. https://doi.org/10.1117/12.2011406.

[6] M. Matsunobu, T. Nishiyama, michio Inoue, R. Housley, C. Bozdog, J. Lim, B. Watson, J. Reece, S. McCandless, O. Zwier, M. van der Schaar, M. Bozkurt, M. al Arif, E. McNamara, P. Kapel, A. Khan, S. Strom, P. Turner, P. Olson, E. van West, Novel diffraction based overlay metrology utilizing phase-based overlay for improved

robustness, in: O. Adan, J.C. Robinson (Eds.), Metrol. Insp. Process Control Semicond. Manuf. XXXV, SPIE, Online Only, United States, 2021: p. 71. https://doi.org/10.1117/12.2584759.
[7] H. Lee, H. Chang, H. Shin, O. Choi, Image-based overlay target design using a grating intersection, J. MicroNanopatterning Mater. Metrol. 21 (2022). https://doi.org/10.1117/1.JMM.21.3.034801.
[8] H. Zhang, C. Tabery, R. Maas, O. Khodko, V.M. Blanco Carballo, E. Canga, F. Schleicher, Predictive compact model for stress-induced on-product overlay correction, J. MicroNanopatterning Mater. Metrol. 21 (2022). https://doi.org/10.1117/1.JMM.21.4.043201.
[9] T. Bourguignon, B. Le Gratiet, J. Pradelles, S. Bérard-Bergery, C. Valade, N.G. Schuch, N. Possémé, High-spatial frequency on-device overlay characterization using CD-SEM contours, in: J.C. Robinson, M.J. Sendelbach (Eds.), Metrol. Insp. Process Control XXXVII, SPIE, San Jose, United States, 2023: p. 16. https://doi.org/10.1117/12.2657914.
[10] T. Bourguignon, R. Bouyssou, J. Pradelles, S. Bérard-Bergery, B. Le-Gratiet, R. Bange, N.G. Schuch, T. Figueiro, N. Possémé, Enabling on-device and target-free overlay measurement from CD-SEM contours, in: J.C. Robinson, M.J. Sendelbach (Eds.), Metrol. Insp. Process Control XXXVI, SPIE, San Jose, United States, 2022: p. 26. https://doi.org/10.1117/12.2613327.
[11] F. Yeh, H. Chouaib, Scatterometry and machine learning for in-die overlay solution, in: J.C. Robinson, M.J. Sendelbach (Eds.), Metrol. Insp. Process Control XXXVII, SPIE, San Jose, United States, 2023: p. 98. https://doi.org/10.1117/12.2657946.
[12] D.F. Sunday, S. List, J.S. Chawla, R.J. Kline, Determining the shape and periodicity of nanostructures using small-angle X-ray scattering, J. Appl. Crystallogr. 48 (2015) 1355–1363. https://doi.org/10.1107/S1600576715013369.
[13] D.F. Sunday, F. Delachat, A. Gharbi, G. Freychet, C.D. Liman, R. Tiron, R.J. Kline, X-ray characterization of contact holes for block copolymer lithography, J. Appl. Crystallogr. 52 (2019) 106–114. https://doi.org/10.1107/S1600576718017272.
[14] W. Wu, R.J. Kline, R.L. Jones, H.-J. Lee, E.K. Lin, D.F. Sunday, C. Wang, T. Hu, C.L. Soles, Review of the key milestones in the development of critical dimension small angle x-ray scattering at National Institute of Standards and Technology, J. MicroNanopatterning Mater. Metrol. 22 (2023) 031206. https://doi.org/10.1117/1.JMM.22.3.031206.
[15] J. Reche, Y. Blancquaert, G. Freychet, P. Gergaud, M. Besacier, Dimensional Control of Line Gratings by Small Angle X-Ray Scattering: Shape and Roughness Extraction, in: 2020 31st Annu. SEMI Adv. Semicond. Manuf. Conf. ASMC, IEEE, Saratoga Springs, NY, USA, 2020: pp. 1–6. https://doi.org/10.1109/ASMC49169.2020.9185351.
[16] J. Reche, P. Gergaud, Y. Blancquaert, M. Besacier, G. Freychet, Shape and Roughness Extraction of Line Gratings by Small Angle X-Ray Scattering: Statistics and Simulations, IEEE Trans. Semicond. Manuf. 35 (2022) 425–431. https://doi.org/10.1109/TSM.2022.3176026.
[17] O. Sorkhabi, J. Zhang, D. Hu, A. Aiyiti, Y.-Y. Lin, M. Li, H.Q.T. Bui, D. Oak, P. Da, Z. Tan, Flash memory hole etch profile monitoring using x-ray and optical scatterometry, J. MicroNanopatterning Mater. Metrol. 22 (2023). https://doi.org/10.1117/1.JMM.22.3.031207.
[18] P. Gin, M. Wormington, Y. Amasay, I. Grinberg, A. Brady, I. Reichental, K. Matney, J. Zhang, O. Sorkhabi, Inline metrology of high aspect ratio hole tilt and center line shift using small-angle x-ray scattering, J. MicroNanopatterning Mater. Metrol. 22 (2023). https://doi.org/10.1117/1.JMM.22.3.031205.
[19] R.J. Kline, D.F. Sunday, D. Windover, B.D. Bunday, X-ray scattering critical dimensional metrology using a compact x-ray source for next generation semiconductor devices, J. MicroNanolithography MEMS MOEMS 16 (2017) 014001. https://doi.org/10.1117/1.JMM.16.1.014001.
[20] A. Veldman, Methods and apparatus for measuring semiconductor device overlay using X-ray metrology, US 2015/0117610 A1, 2015.
[21] J. Zhang, X. Chen, T. Yang, S. Liu, X-ray-based overlay metrology using reciprocal space slicing analysis, Opt. Lett. 48 (2023) 6380 – 6383. https://doi.org/10.1364/OL.505346.
[22] E. Sezestre, J. Scoarnec, J. Pradelles, L. Perraud, A. Fay, S. Bérard-Bergery, J. Bustos, J.-B. Henry, O. Dubreuil, I. Mendes, C. Valade, A. Moly, A. Batte, N.G. Schuch, F. Robert, T. Figueiro, Model-based contour extraction: an enabler for very low-frame SEM images metrology, in: J.C. Robinson, M.J. Sendelbach (Eds.), Metrol. Insp. Process Control XXXVI, SPIE, San Jose, United States, 2022: p. 75. https://doi.org/10.1117/12.2616527.
[23] O. Inoue, K. Hasumi, Review of scanning electron microscope-based overlay measurement beyond 3-nm node device, J. MicroNanolithography MEMS MOEMS 18 (2019) 1. https://doi.org/10.1117/1.JMM.18.2.021206.
[24] O. Inoue, T. Kato, Y. Okagawa, H. Kawada, In-die overlay metrology by using CD-SEM, in: A. Starikov, J.P. Cain (Eds.), San Jose, California, USA, 2013: p. 86812S. https://doi.org/10.1117/12.2011035.

[25] B.L. Gratiet, R. Bouyssou, J. Ducoté, A. Ostrovsky, S. Audran, C. Gardin, N.G. Schuch, C. Valade, J. Belissard, M. Millequant, T. Figueiro, P. Schiavone, Pattern placement and shape distortion control using contour-based metrology, in: Metrol. Insp. Process Control Semicond. Manuf. XXXV, SPIE, 2021: pp. 182–194. https://doi.org/10.1117/12.2584364.
[26] E. Soltani, B. Le-Gratiet, S. Bérard-Bergery, J. Pradelles, R. Bange, N. Schuch, T. Figueiro, R. Tiron, Highlighting stochastic manifestations in 193 nm immersion lithography with contour-based metrology metrics, in: Metrol. Insp. Process Control XXXVI, SPIE, 2022: pp. 45–58. https://doi.org/10.1117/12.2613322.
[27] K. Hasumi, O. Inoue, Y. Okagawa, C. Shao, P. Leray, S. Halder, G. Lorusso, C. Jehoul, SEM-based overlay measurement between via patterns and buried M1 patterns using high-voltage SEM, in: M.I. Sanchez, V.A. Ukraintsev (Eds.), San Jose, California, United States, 2017: p. 101451J. https://doi.org/10.1117/12.2257848.
[28] B.L. Gratiet, R. Bouyssou, J. Ducoté, C. Dezauzier, A. Ostrovsky, C. Beylier, C. Gardin, P. Petroni, M. Milléquant, A. Chagoya-Garzon, P. Schiavone, Contour based metrology: getting more from a SEM image, in: Metrol. Insp. Process Control Microlithogr. XXXIII, SPIE, 2019: pp. 332–340. https://doi.org/10.1117/12.2511626.
[29] J.N. Sarvaiya, S. Patnaik, S. Bombaywala, Image Registration by Template Matching Using Normalized Cross-Correlation, in: 2009 Int. Conf. Adv. Comput. Control Telecommun. Technol., 2009: pp. 819–822. https://doi.org/10.1109/ACT.2009.207.
[30] G. Freychet, G.J. Rademaker, Y. Blancquaert, P. Gergaud, Reconstruction of the in-depth profile of line gratings with critical dimension grazing incidence small angle x-ray scattering on a laboratory equipment, in: J.C. Robinson, M.J. Sendelbach (Eds.), Metrol. Insp. Process Control XXXVII, SPIE, San Jose, United States, 2023: p. 53. https://doi.org/10.1117/12.2657500.
[31] T. Choisnet, A. Hammouti, V. Gagneur, J. Reche, G. Rademaker, G. Freychet, G. Jullien, J. Ducote, P. Gergaud, D. Le Cunff, Critical dimension measurement: from synchrotron small angle x-ray scattering to industrial optical scatterometry techniques, in: J.C. Robinson, M.J. Sendelbach (Eds.), Metrol. Insp. Process Control XXXVII, SPIE, San Jose, United States, 2023: p. 52. https://doi.org/10.1117/12.2657661.
[32] G. Freychet, D. Kumar, R.J. Pandolfi, P. Naulleau, I. Cordova, P. Ercius, C. Song, J. Strzalka, A. Hexemer, Estimation of Line Cross Sections Using Critical-Dimension Grazing-Incidence Small-Angle X-Ray Scattering, Phys. Rev. Appl. 12 (2019) 044026. https://doi.org/10.1103/PhysRevApplied.12.044026.
[33] A.F. Hannon, D.F. Sunday, D. Windover, R. Joseph Kline, Advancing x-ray scattering metrology using inverse genetic algorithms, J. MicroNanolithography MEMS MOEMS 15 (2016) 034001. https://doi.org/10.1117/1.JMM.15.3.034001.
[34] F.-A. Fortin, DEAP: Evolutionary Algorithms Made Easy, (n.d.).
[35] N. Hansen, A. Ostermeier, Completely derandomized self-adaptation in evolution strategies, Evol. Comput. 9 (2001) 159–195. https://doi.org/10.1162/106365601750190398.